Matthew Proctor*, Paloma A. Huidobro, Stefan A. Maier, Richard V. Craster
and Mehul P. Makwana

Manipulating topological valley modes in plasmonic metasurfaces

Abstract: Coupled light-matter modes supported by plasmonic metasurfaces can be combined with topological principles to yield subwavelength topological valley states of light. This study gives a systematic presentation of the topological valley states available for lattices of metallic nanoparticles (NPs): all possible lattices with hexagonal symmetry are considered as well as valley states emerging on a square lattice. Several unique effects that have yet to be explored in plasmonics are identified, such as robust guiding, filtering, and splitting of modes, as well as dual-band effects. These are demonstrated by means of scattering computations based on the coupled dipole method that encompass full electromagnetic interactions between NPs.

Keywords: metal nanoparticles; plasmonic metasurface; topological nanophotonics; topological plasmonics; topological valley modes.

1 Introduction

Plasmonics offers a unique platform for controlling light on the nanoscale [1]. Coherent electron oscillations known

as localized surface plasmons arise when light interacts with metallic nanostructures. These localized excitations confine light beyond the diffraction limit and have optical properties tunable by the size, material, and shape of the nanostructures that host them as well as the surrounding environment [2]. This has resulted in a plethora of applications, including the waveguiding of light on the nanoscale [3] and the exploration of chiral optical interactions with surface plasmon polaritons [4]. Notably, owing to advances in nanofabrication, unexpectedly long propagation lengths of surface plasmons in waveguides have been reported [5].

Plasmonic metasurfaces, which are collections of plasmonic nanoparticles (NPs) in a plane arranged in different lattices, are the subject of current intense research due to their enriched properties leveraged by the flexibility in geometrical designs [6]. Exploiting the radiative coupling regime between NPs [7], whose interactions are mediated by diffractive modes in the plane of the array (surface lattice resonances), has enabled the experimental demonstration of lasing [8, 9] and Bose-Einstein condensation [10] in plasmonic lattices due to their dramatic quality factor enhancement. In contrast, the near-field coupling regime, where the distance between NPs is very subwavelength, is currently regaining interest due to the possibility of realizing topological phases of light confined at nanoscale dimensions using metal NPs as well as other nanoresonators such as dielectric NPs [11–19]. This has been sparked by the potential of topological protection to provide robust light propagation immune to certain kinds of disorder and imperfections in samples, in analogy to the effects present in topological insulators, materials that are insulating in the bulk and possess protected conduction states along their edge [20].

Topological insulators have unidirectional edge states where backscattering is entirely suppressed in the absence of magnetic impurities, as there is no backward propagating mode to couple into. These states are reliant on the fractional spin of fermions. Therefore, although these electronic systems have inspired research into bosonic analogues, they require alternative strategies for creating topological states [21–23]. Unidirectional (i.e. nonreciprocal) edge states can be obtained for photons by breaking

---

*Corresponding author: Matthew Proctor, Department of
Mathematics, Imperial College London, London SW7 2AZ, UK,
e-mail: matthew.proctor12@imperial.ac.uk.
https://orcid.org/0000-0002-5356-9917
Paloma A. Huidobro: Instituto de Telecomunicações, Insituto
Superior Tecnico-University of Lisbon, Avenida Rovisco Pais 1,
1049-001 Lisboa, Portugal
Stefan A. Maier: Chair in Hybrid Nanosystems, Nanoinstitut
München, Faculty of Physics, Ludwig-Maximilians-Universität
München, 80539 München, Germany; and Department of Physics,
Imperial College London, London SW7 2AZ, UK
Richard V. Craster: Department of Mathematics, Imperial College
London, London SW7 2AZ, UK
Mehul P. Makwana: Department of Mathematics, Imperial College
London, London SW7 2AZ, UK; and Multiwave Technologies AG,
3 Chemin du Prê Fleuri, 1228 Geneva, Switzerland

time-reversal symmetry through the use of strong magnetic fields [24, 25]. However, there are constraints in miniaturizing this approach to nanoscale set-ups, and there is a need for alternative designs.

Topological valley (Hall) modes are solely reliant on energy extrema in reciprocal space, and they form a specific subclass not contingent upon particles with fractional spin or a time-reversal breaking component [26]. Although they are not completely protected against backscattering, the existence of a local, valley-dependent topological invariant means that these states do inherit some aspects of topological protection [26]. An advantage of these topological valley modes is that they only require the breaking of an inversion and/or a mirror symmetry; consequently, topological valley states in plasmonics enable more robust plasmonic modes while remaining within reach of current experimental set-ups. Existing work on topological valley effects in photonics has focused on hexagonal and triangular structures [27–31]. In plasmonics, graphene has been proposed to host topological valley modes at infrared frequencies by imposing a triangular structured doping landscape on a graphene sheet using a metagate [32], and designer (spoof) plasmons are used to experimentally probe these effects at microwave frequencies [33].

This paper shows that a two-dimensional (2D) lattice of metallic NPs provides a versatile platform for demonstrating the existence of topological valley states in plasmonics. The symmetry requirements for these states are discussed and a systematic description of the topological valley states available is presented. Existing cases in the literature have used hexagonal (C_{6v}) and triangular (C_{3v}) symmetry-induced Dirac cones, and they have each, respectively explored a single edge configuration. Here, all possible edge configurations with these symmetries have been classified [34, 35]. Additionally, a square lattice with C_{4v} is presented in the Supplementary Material. From the properties of the edge states, networks of regions, composed of various symmetry types, have been designed to engineer advanced waveguiding techniques such as filtering, evanescent coupling, and splitting at subwavelength scales.

2 Methods

In this paper, we study topological valley modes in 2D lattice of spheroidal, silver NPs (Figure 1C). The system is modelled using the coupled dipole method (CDM). The permittivity of NPs is described with the Drude model:

$$\varepsilon(\omega)=\varepsilon_\infty-\frac{\omega_p^2}{\omega^2+i\omega\gamma} \tag{1}$$
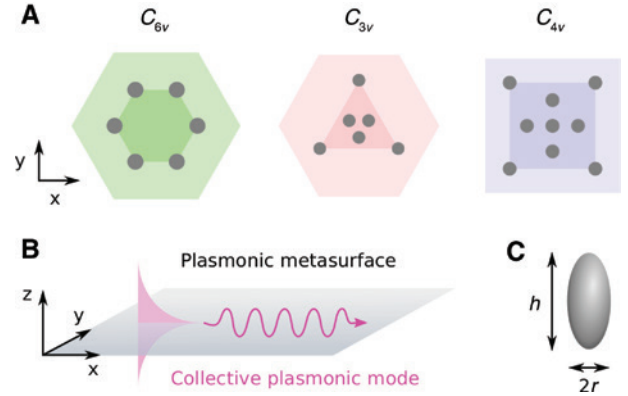

Figure 1: Set up of the system.
(A) Unit cells with C_{6v}, C_{3v}, and C_{4v} symmetries. The shading indicates shapes with equivalent symmetries. (B) Plasmonic metasurface: Collective plasmonic resonances arise from the coupling between localized surface plasmons on each NP; they propagate in 2D metasurface and decay exponentially perpendicular to the plane of the metasurface. (C) Spheroidal NPs, with in-plane radius r and height h, host a dipole moment out-of-the-plane, p_z, decoupled from the in-plane dipole moment.

where $\varepsilon_\infty=5$, $\omega_p=8.9$ eV, and $\gamma=38$ meV [36]. For each lattice arrangement, it is assumed that the NP in-plane radius r, height h, nearest-neighbor spacing R, and lattice constant a_0 are all subwavelength. It is ensured that $R>3r$, which allows NPs to be treated as point dipoles, as higher-order resonances can be neglected [37]. The interaction between multiple NPs is described by Green's function (see Supplementary Material). The in-plane and out-of-plane polarizations are orthogonal and furthermore become well separated in frequency for spheroidal NPs, with in-plane modes shifting to higher frequencies and out-of-plane-modes shifting to lower frequencies. This means that they can be investigated separately [38]; here, only out-of-plane polarized modes corresponding to dipole moments perpendicular to the xy-plane of the metasurface are considered (Figure 1B). The long-range terms in Green's function are responsible for retarded interactions, which can have remarkable effects in plasmonics [37] and in particular in topological plasmonics, where bulk-edge correspondence can break down due to retardation [39]. However, this work is limited to very subwavelength arrays of NPs where near-field interactions dominate.

3 Designing topological valley states

3.1 Engineering Dirac cones

In designing topological valley states, a process of engineering a Dirac cone and then breaking it is followed. Dirac

cones are degeneracies in the band structure of a system, which disperse linearly and can be described by an effective Dirac Hamiltonian. This conical dispersion leads to a number of interesting transport phenomena [40]. Topological valley states rely on the existence of valleys, energy extrema around a lifted Dirac degeneracy, in the band structure. A large separation of two valleys in the Brillouin zone (BZ) allows a local, valley-dependent topological invariant to be defined: the valley-Chern number [41]. This quantity is calculated from the Berry curvature, which is strongly localized at the valleys provided the perturbation, which breaks the Dirac cone, is small enough [26]. A large perturbation results in the Berry curvature becoming less localized and the topological valley effect is diminished. Although locally defined, the valley-Chern number has been shown to guarantee the existence of edge states for a host of systems [42] as a result of the bulk boundary correspondence [26]. The properties of these edge states are discussed in Section 3.2.

The existence of a Dirac cone is dependent on the crystal symmetry of the system. In plasmonics, the existing literature has focused on hexagonal, graphene-like arrangements of NPs [38, 43], where deterministic Dirac cones appear at K and K' points in the BZ and are protected by the C_{3v} symmetry of these points [34, 40]. Extending beyond these simple lattices, group theoretical rules for the existence of Dirac cones are followed. As the symmetries in the BZ are linked to the real space arrangement of NPs, these rules determine the lattices that can be used. A more in-depth discussion of the symmetries are given in Supplementary Material. In this paper, three types of unit cells are considered, with the symmetries shown in Figure 1A. In the following, these are referred to by their pre-perturbation symmetry, C_{3v}, C_{6v}, and C_{4v}.

Although group theoretical concepts predict the presence of Dirac cones [44], the frequency at which they occur is dependent on the interaction matrix of the system. Provided the cellular structure satisfies the required symmetries, there exists a freedom in the choice of other parameters such as the radius, number, and type of NPs. Similarly, there is flexibility when breaking the Dirac cone. The degree of symmetry breaking by changes in the orientation, size, and material properties of these elements all influence the width of the band gap. In this regard, system parameters must be tuned to ensure that, once the degeneracy is broken, a band gap across the whole BZ is achieved. Importantly, the guidelines espoused herein are applicable to any nanophotonic or plasmonic system, such as arrangements of dielectric NPs or periodically doped graphene.

Figure 2A and B shows the unit cell for the C_{3v} case before (and after) the perturbation where the mirror symmetry σ_v is removed by a rotation. In Figure 2D and E, the band structures, including all neighbors in a QSA, are plotted. Upon symmetry reduction, the Dirac cone is opened resulting in a complete band gap (blue). In Figure 2F and G, the system, including retardation and radiative effects, is characterized, and the spectral function is plotted [45]. As the NP and lattice parameters are very subwavelength, the QSA accurately describes the behavior of the lower-energy bands, although it does not capture the polariton splitting at the light line of the highest-energy band. In these plots, Drude losses $\gamma = 10$ meV are chosen for clarity, and results for material losses in silver, $\gamma = 38$ meV, are given in the Supplementary Material.
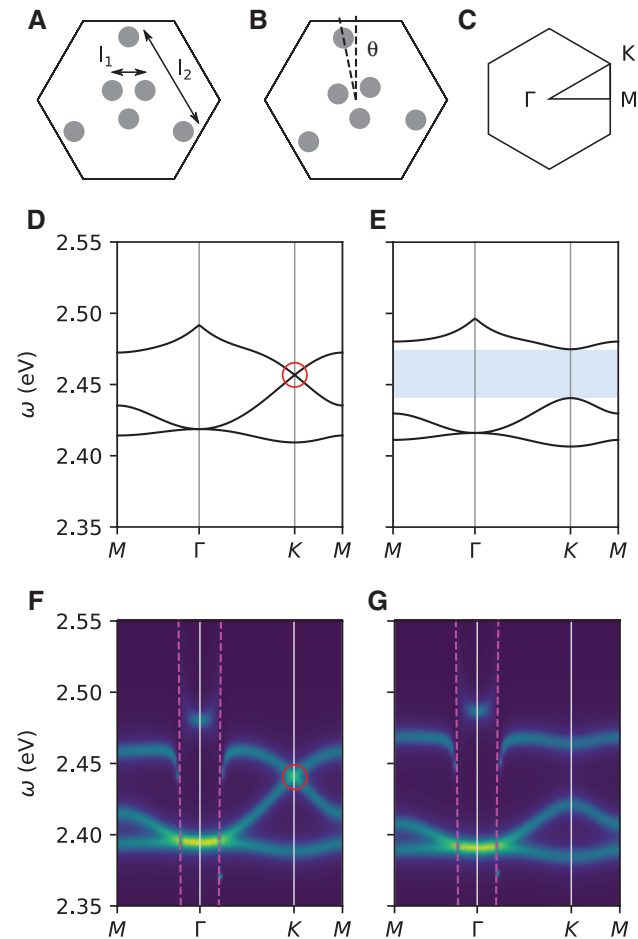

Figure 2: C_{3v} case.
(A) Unit cell with NP radius $r = 5$ nm and height $h = 30$ nm, internal spacing $l_1 = 10\sqrt{3}$ nm, external spacing $l_2 = 30\sqrt{3}$ nm, and lattice constant $a_0 = 75$ nm. (B) A $\theta = 0.1$ rad rotation removes σ_v. (C) BZ. (D) Band structure, pre-perturbation. (E) Post-perturbation. (F and G) Spectral function: Higher-energy bands experience polariton-like splitting at the light line (magenta). Drude losses $\gamma = 10$ meV.

Three additional bands, at higher and lower energies, are also present in this system, as there are six elements in the unit cell. As they are not in the vicinity of the Dirac cone, the authors choose not to show them. A particular advantage of this lattice is that only a single type of NP is used, which makes fabrication more straightforward.

Figure 3A and B shows the band structure for the C_{6v} case, with $\gamma = 38$ meV. For this case, both σ_v and inversion symmetry must be broken to gap the Dirac cone. This is achieved by perturbing the radius of alternating NPs in the unit cell by $\pm\delta r$. The height of NPs is fixed. Only the spectral function is plotted, as the quasistatic eigenvalue problem becomes nonlinear as a result of employing spheroids of different sizes. Note that this case is similar to transition metal dichalcogenides and hexagonal boron nitride, which naturally have broken inversion symmetry unit cells due to their bipartite lattice structures with different atoms. Unlike the C_{3v} case, here, there are two Dirac cones at different frequencies, which both result in a complete band gap once they are opened. Previous plasmonic topological valley systems have solely focused on single band effects, but such a dual-band structure allows topological valley states to exist in two frequency regimes. Dual-band effects have also been demonstrated in photonic crystals [46] and acoustics [47].

Dirac cones are only guaranteed for these triangular and hexagonal lattices. However, there are other instances

where Dirac cones can be engineered along high-symmetry lines [48–50]. Notably, irrespective of whether the Dirac cone is symmetry induced or not, there remains a nontrivial valley-Chern number defined in the vicinity of the degeneracy [49]. An example of a plasmonic metasurface possessing these properties is given in the Supplementary Material.

3.2 Edge states

In this subsection, edge states that reside in the band gaps generated in the previous subsection are investigated. The bulk boundary correspondence guarantees the existence of topological valley edge states between topologically distinct regions characterized by valley-Chern numbers with opposite sign [26, 51]. Trivial edge states are also possible between regions with the same valley-Chern number. Table 1 summarizes the perturbations of two regions, A and B, which generate nontrivial and trivial edge states. There are, at most, three geometrically distinct interfaces possible for each of the triangular-based structures. For each of these cases, there will be two inequivalent interfaces A/B and B/A that yield different eigenstates.

The existing literature in plasmonics on topological valley effects solely considers one of the three distinct interfaces that are possible [32, 33], specifically type I case, as shown in Table 1. Herein, the realization of the topological type II edge states in the C_{3v} system reveals features that have yet to be discussed in the context of plasmonics. Also, although trivial type III edge states are not guaranteed to exist, they do here for this choice of parameters (see Supplementary Material). Notably, C_{3v} and C_{6v} type I cases are mathematically identical to the canonical honeycomb structure, which has been the subject of other works [31, 52], as they share the same symmetries.

To numerically simulate the edge states, a ribbon of hexagons is set up and Bloch periodicity is set across the ribbon. The interactions between NPs include all
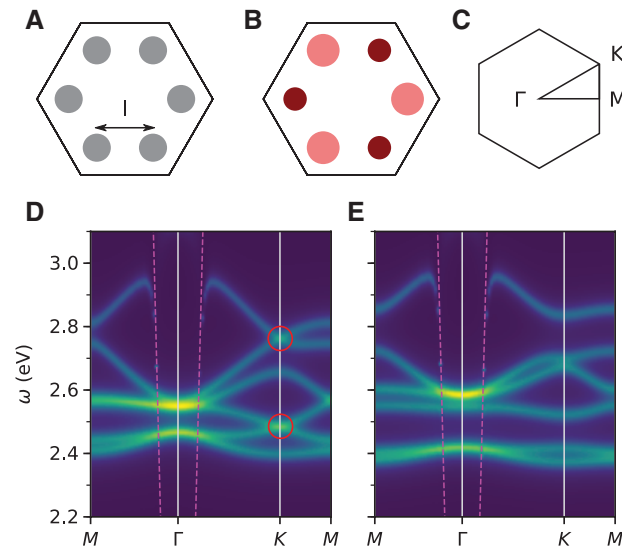

Figure 3: C_{6v} case.
(A) Unit cell with NP radius $r = 6$ nm and height $h = 30$ nm, nearest-neighbor spacing $l = 24$ nm, and lattice constant $a_0 = 65$ nm.
(B) Alternating NPs are perturbed by $\delta r = \pm 0.5$ nm, with the height remaining constant. (C) BZ. (D and E) Spectral function: Highest-energy band experiences polariton-like splitting. Drude losses $\gamma = 38$ meV.

Table 1: C_{3v} interfaces: summary of the different interface types, including the perturbations of regions A and B and properties of each edge state.

Type	A	B	Properties
I	$+\theta$	$-\theta$	Two edge states propagating in opposite directions
II	$+\theta$	$+\theta + \dfrac{\pi}{3}$	Edge states on only one interface
III	$+\theta$	$-\theta + \dfrac{\pi}{3}$	Two nearly degenerate edge states on both interfaces

neighbors in a QSA. Along the finite direction, region A is clad with region B on the top and bottom to capture both interfaces A/B and B/A. Each region is n=10 unit cells long to ensure that edge states at each interface decay within the length of the ribbon. At each end of the ribbon, a hard boundary condition with the vacuum is chosen. Edge states that appear at this boundary are not topological (as the valley-Chern number of the vacuum is zero); these are removed from the band structures.

Figure 4 shows the band structure for C_{3v}, type I edges. There are two overlapping edge states across the band gap, which exist over the same frequency range. On either side of band structures, dipole moments of the eigenstates of each interface are plotted; these two eigenstates show a clear difference in the pattern of the mode. Along both interfaces, the edge state is very subwavelength and strongly confined.

The band structure for C_{3v}, type II edges is shown in Figure 5. Unlike Figure 4, both edge states now reside on the same interface. They also do not span the band gap due to the size of the perturbation. Although the bands do not span the band gap, they can still be used to filter modes: only A/B interface modes exist in the gap, meaning there are no modes along B/A to couple into.

Finally, Figure 6 shows the band structure for the edge modes in the C_{6v} lattice. As with the bulk band structure, the spectral function is plotted, as the quasistatic eigenvalue problem is nonlinear. The higher-frequency band is shown in Figure 6A and the lower-frequency band in shown in Figure 6B. As the spectral function captures all modes, including those that are at the boundary with the vacuum, the topological edge states on the relevant interfaces are highlighted in white. Both bands possess counterpropagating edge states, which are exploited in Section 4.
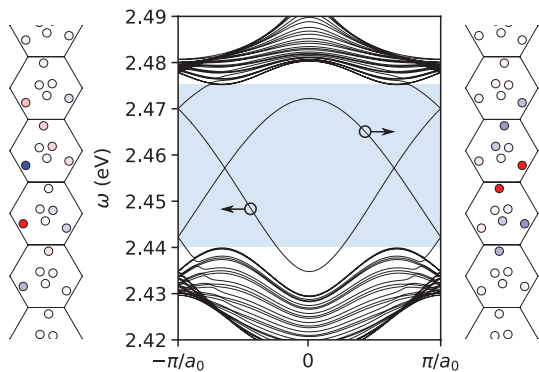

Figure 5: C_{3v}, type II edge.
The top and bottom media are perturbed by $\theta = \pm 0.1$ and $\theta = +0.1 + \frac{\pi}{3}$ rad, respectively. Only modes of one interface are present in the bulk band gap and the dipole moments of these modes are shown either side.

Figure 6: C_{6v}, type I edge.
The top and bottom media differ by an inversion about the vertical. Edge states reside in both (A) top band gap and (B) bottom band gap. Relevant topological edge states are highlighted on the right in white.

3.3 Elements of topological protection

Topological insulators that break time-reversal symmetry have strictly unidirectional edge states. In contrast, the presence of time-reversal symmetry for the system results in bidirectional edge states; hence, backscattering is not entirely prohibited. Despite this, there are still elements

Figure 4: C_{3v}, type I edge.
The top and bottom media are perturbed by $\theta = \pm 0.1$ rad. Band structure for the edge states. The dipole moments of the edge states circled are shown either side, demonstrating the confinement to the edge.
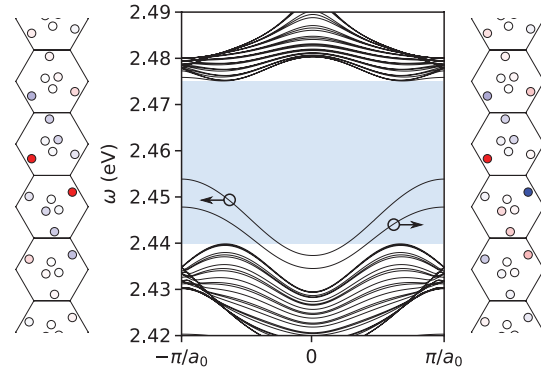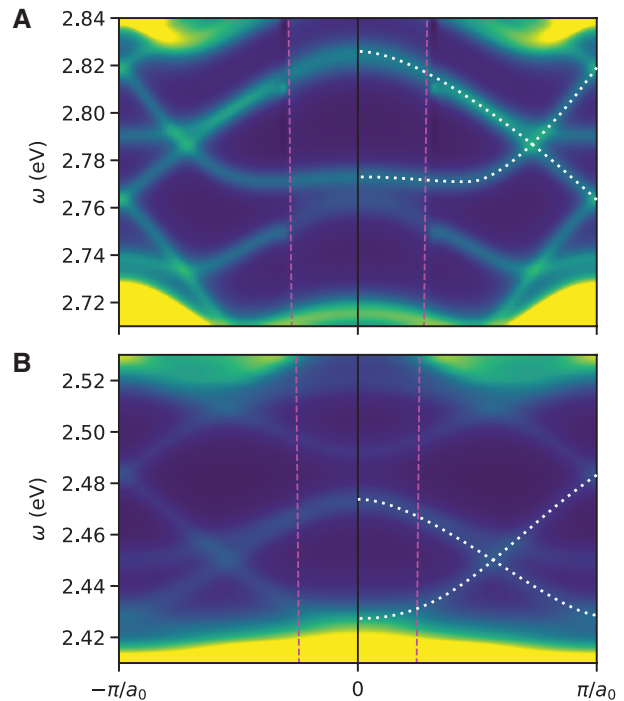
that contribute to these states having a degree of protection that allows them to be used to efficiently guide light.

A mode with a particular chirality will not readily couple with one of opposite chirality, giving it protection against a disorder that does not cause the chirality to switch. Quantities that characterize spin and chirality are calculated to emphasize the difference between the topologically trivial and nontrivial edge states. The time-averaged Poynting vector $\mathbf{S} = \frac{1}{2}\mathrm{Re}(\mathbf{E} \times \mathbf{H}^*)$ characterizes the flow of electromagnetic energy in a system. In Figure 7, the Poynting vector (arrows) for a nontrivial, type I edge state and a trivial, type III edge state is plotted. In the nontrivial case, the curl of the Poynting vector is nonzero whereas in the trivial case the curl is mostly zero. The out-of-plane component of the spin angular momentum $T_z = \mathrm{Im}(\mathbf{H}^* \times \mathbf{H})_z$ in the plane of the metasurface (color) is also plotted, as in dispersive, inhomogeneous media, this quantity provides a more appropriate description of chiral light-matter interactions [53]. Again, in the nontrivial case, the normalized magnitude of the spin angular momentum is much greater than the trivial case.

The presence of backscattering in topological valley states is also intimately linked to the separation of forward and backward propagating modes in Fourier space [34]. In the C_{3v} and C_{6v} cases discussed in Section 3.1, after breaking the necessary symmetries, valleys at K/K' are well separated in Fourier space, as they are at the edges of the BZ. In contrast, in systems with Dirac points engineered along high-symmetry lines, rather than high-symmetry points, such as the C_{4v} system, valleys will not be maximally separated (see Supplementary Material). This results in these systems being more susceptible to backscattering. Despite this, there are means in which to expand the Fourier separation, the separation between opposite valleys in reciprocal space, for this particular case [50]. Notably, armchair-type edges in triangular lattices also have a small Fourier separation relative to their zigzag counterparts. However, unlike the C_{4v} system, considered here, the valleys are completely coupled in the vicinity of Γ resulting in an anticrossing and enhanced backscattering [54].

Other popular designs, such as the proposal in Ref. [55], also suffer from this; there, an extended honeycomb lattice unit cell is used to emulate the quantum spin Hall effect. However, the larger unit cell results in the folding of the K/K' valleys onto Γ, thereby inhibiting the protection afforded by a larger Fourier separation. Additionally, upon the introduction of an interface, the C_6 reliant pseudospin states couple to each other resulting in an anticrossing near Γ. These properties result in reduced protection against positional disorder; hence, these modes are far less robust than the topological valley modes considered here [56].

4 Topological valley networks

Using the topological valley edge states, topological networks can be designed [34]. These are formed by joining geometrically distinct regions of the various symmetry types. We first show this for the C_{3v} then the C_{6v} system, and include the C_{4v} case in the Supplementary Material.

In the following, full electromagnetic interactions between NPs using the retarded, radiative Green's function are included. The absolute value of the real part of the dipole moment for each NP in the lattice is plotted. To make the edge states more visible, the radius of NPs in the plots is increased, but this does not change the physical system. In each case, a particular NP in the respective lattice located near an interface, which triggers a mode to propagate along the interface on which it sits, is excited. Initially, the Drude losses are set to zero to fully expose the behavior of the edge states. To prevent the mode reflecting off the hard boundary with the vacuum, losses toward these boundaries are increased gradually. As the topologically nontrivial edge states possess a chirality, a circularly polarized magnetic dipole source external to the lattice could also be used to excite unidirectional modes, where the direction is determined by the spin angular momentum at the source position [16].
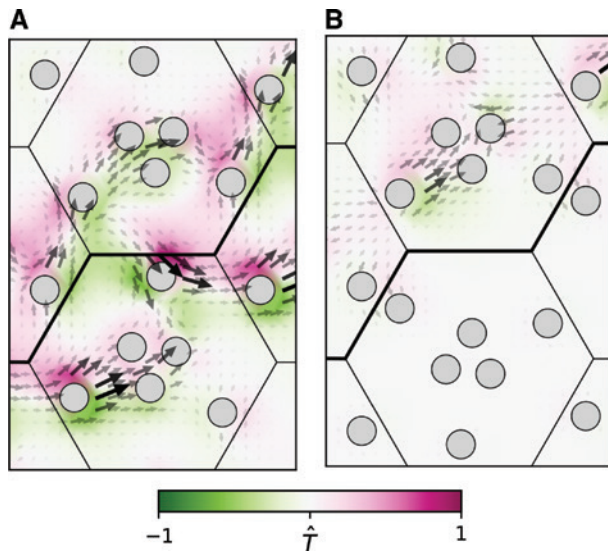

Figure 7: Chirality comparison: Poynting vector **S** (arrows) and normalized spin angular momentum (color) $\hat{T}_z$.
(A) Nontrivial edge mode on C_{3v}, type I edge. (B) Trivial edge mode on C_{3v}, type III edge: energy flow is more linear, as seen in the small spin angular momentum amplitude.

A junction of the C_{3v}, type I system is shown in Figure 8A and B. The semianalytical CDM gives clarity to the dipole moment mode patterns along each lead, which correspond to the edge states calculated in Figure 4. The patterns along lead 1 and lead 2 are identical, but they differ from lead 3, which highlights the different interfaces A/B and B/A as shown in Figure 8A. The A/B mode is able to couple into the B/A mode at the junction due to the overlapping edge states. Despite this, the mode does not propagate straight through along lead 4, as it has opposite chirality and a wavevector mismatch [34].

To highlight the robustness of this junction, the time-averaged Poynting flux through each of the exit leads ϕ_i as a fraction of the flux along the entry lead ϕ_1 is calculated.

In the frequency range where both interface modes are excitable, the majority of energy flows along lead 2. The blue region between leads 1 and 3 in Figure 8A introduces a barrier to energy flow; similar effects have been observed in other systems [33] and the importance of the nodal region has been highlighted in Ref. [34]. Importantly, over the majority of the band gap, ϕ_{out}, the fraction of output over input energy is ~1. As shown in Figure 4, the topological valley bands do not reach the top of the band gap causing $\phi_{out}<1$ at higher frequencies. Note that the band gap is shifted ~0.02 eV compared to the quasistatic
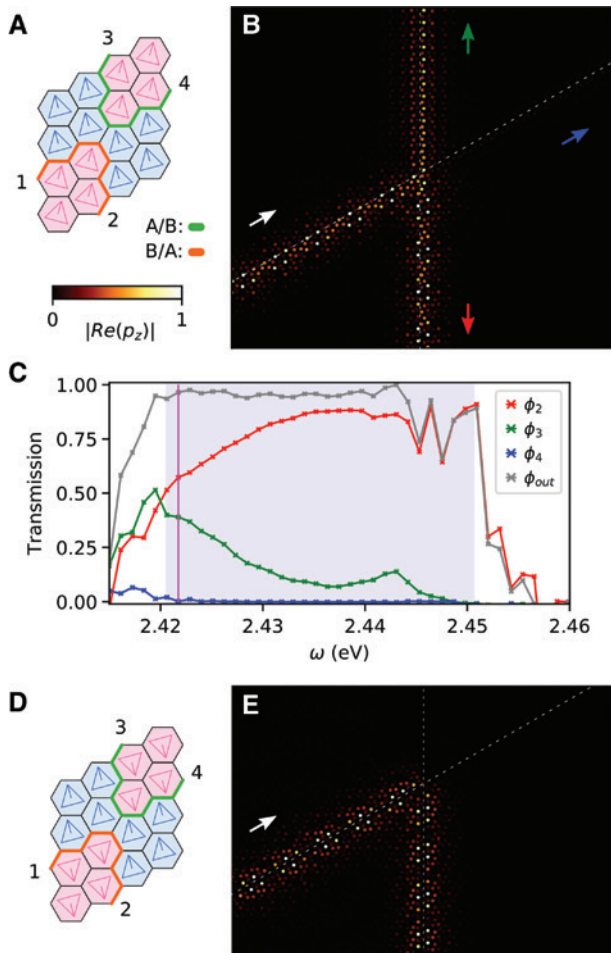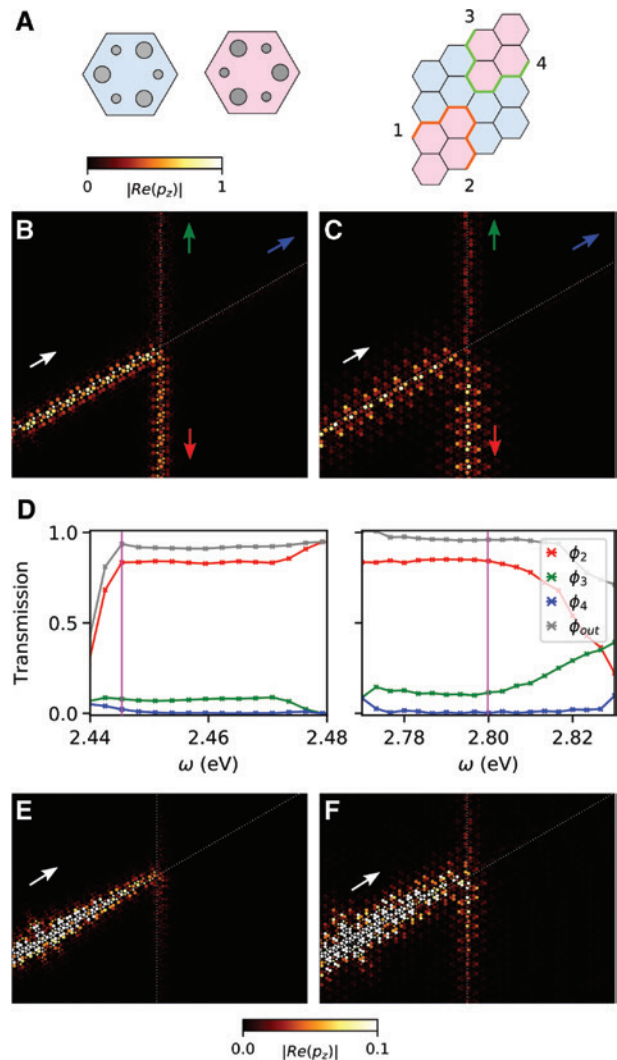

Figure 8: Topological waveguiding with C_{3v} networks. (A) Type I: two-way splitting junction. (B) $\omega = 2.421$ eV. The mode along lead 1 splits at the junction, propagating around the gentle $2\pi/3$ (lead 3) and sharp $\pi/3$ (lead 2) bends. (C) Transmission ϕ along each lead. The band gap is highlighted in blue. (D) Type II: filtering junction. (E) $\omega = 2.426$ eV. The mode only propagates around the sharp $\pi/3$ bend, owing to there being no mode, at this frequency, along the other interface to couple into.

Figure 9: Dual-band waveguiding with C_{6v} networks. (A) Diagram of the unit cells and two-way splitting junction. (B) $\omega = 2.800$ eV. The mode propagates around both gentle and sharp bends, with almost zero propagation along lead 4. (C) $\omega = 2.446$ eV. The mode also propagates and splits at lower frequencies. (D) Transmission ϕ along each lead over the frequencies at which topological modes are excited for lower- and higher-frequency bands. (E and F) Modes excited at the same frequency as (A and B), including Drude losses $\gamma = 10$ meV.

band structure due to the radiative correction to the polarizability.

Filtering using the C_{3v} type II system is shown in Figure 8D and E. When the mode along lead 1 reaches the junction, it only propagates around the sharp $\pi/3$ bend, owing to the identical interfaces along leads 1 and 2, as seen in the identical mode patterns. As shown in Figure 5, there are only edge states in the band gap corresponding to the B/A interface. Therefore, unlike the type I edge, there is no mode to couple into along lead 3 at this frequency resulting in this filtering effect.

The previous two examples have a specific choice of nodal region at which the different regions intersect, which limits the splitting of a mode, in the type I case, into two directions only. By carefully choosing the arrangement of this intersection point, it is possible to realize topological four-way splitting as well as trivial five-way splitting of a mode [34]. Examples of both of these effects are shown in the Supplementary Material.

Next is waveguiding with the C_{6v} edge states. Networks are set up with the unit cell arrangements shown in Figure 9A. In Figure 9B, a mode is excited along lead 1 in the top band gap of the system. As with the C_{3v} type I edge states, the mode splits at the junction and the mode patterns confirm the distinct interfaces. Figure 9 shows that the lower band edge states also possess the same splitting properties. The Poynting flux through each of the leads as a fraction of the flux through the entry lead is shown in Figure 9D for the frequencies at which topological modes are excited. As with the C_{3v} case, the fraction of output transmission over input is ~1 for the topological modes. In addition, after studying in detail the behavior of the topological valley state, the effect of losses on an interface for the C_{6v} case with $\gamma = 10$ meV, which cause the edge state propagation to become attenuated, is shown in Figure 9E and F.

5 Conclusion

The existence of subwavelength, topological valley states in plasmonic metasurfaces has been presented. Using systematic symmetry arguments, this study provides a guide to realize topological valley modes in any nanophotonic system. Extending the existing topological nanophotonic literature, all possible topological valley modes available for hexagonal unit cell systems, which include new nontrivial and trivial edge states, are described. Furthermore, by designing Dirac cones in square lattice systems, emergent three-way energy splitting in a plasmonic metasurface is revealed for the first time. The semianalytical CDM used to model the systems in this work removes

any computational complexity to expose the topological properties and behavior of modes we engineer. The results are, however, general and could be applied also to lower-frequency plasmonics such as periodically doped graphene or graphene islands or spoof surface plasmons.

References

[1] Maier SA. Plasmonics: fundamentals and applications. Springer Science & Business Media, 2007.

[2] Giannini V, Fernández-Domínguez AI, Heck SC, Maier SA. Plasmonic nanoantennas: fundamentals and their use in controlling the radiative properties of nanoemitters. Chem Rev 2011;111:3888–912.

[3] Barnes WL, Dereux A, Ebbesen TW. Surface plasmon subwavelength optics. Nature 2003;424:824–30.

[4] Bliokh KY, Rodríguez-Fortuño FJ, Nori F, Zayats AV. Spin-orbit interactions of light. Nat Photon 2015;9:796–808.

[5] Kress SJ, Antolinez FV, Richner P, et al. Wedge waveguides and resonators for quantum plasmonics. Nano Lett 2015;15:6267–75.

[6] Meinzer N, Barnes WL, Hooper IR. Plasmonic meta-atoms and metasurfaces. Nat Photon 2014;8:889–98.

[7] Wang W, Ramezani M, Väkeväinen AI, Törmä P, Rivas JG, Odom TW. The rich photonic world of plasmonic nanoparticle arrays. Mater Today 2018;21:303–14.

[8] Zhou W, Dridi M, Suh JY, et al. Lasing action in strongly coupled plasmonic nanocavity arrays. Nat Nanotechnol 2013;8:506–11.

[9] Guo R, Nečada M, Hakala TK, Väkeväinen AI, Törmä P. Lasing at K points of a honeycomb plasmonic lattice. Phys Rev Lett 2019;122:013901.

[10] Hakala TK, Moilanen AJ, Väkeväinen AI, et al. Bose-Einstein condensation in a plasmonic lattice. Nat Phys 2018;14:739–44.

[11] Ling C, Xiao M, Chan CT, Yu SF, Fung KH. Topological edge plasmon modes between diatomic chains of plasmonic nanoparticles. Opt Express 2015;23:2021–31.

[12] Downing CA, Weick G. Topological collective plasmons in bipartite chains of metallic nanoparticles. Phys Rev B 2017;95:125426.

[13] Pocock SR, Xiao X, Huidobro PA, Giannini V. Topological plasmonic chain with retardation and radiative effects. ACS Photon 2018;5:2271–9.

[14] Kruk S, Poddubny A, Smirnova D, et al. Nonlinear light generation in topological nanostructures. Nat Nanotechnol 2019;14:126–30.

[15] Wu RP, Zhang Y, Lee KF, Wang J, Yu SF, Fung KH. Dynamic long range interaction induced topological edge modes in dispersive gyromagnetic lattices. Phys Rev B 2019;99:214433.

[16] Proctor M, Craster RV, Maier SA, Giannini V, Huidobro PA. Exciting pseudospin dependent edge states in plasmonic metasurfaces. ACS Photon 2019;6:2985–95.

[17] Slobozhanyuk A, Shchelokova AV, Ni X, et al. Near-field imaging of spin-locked edge states in all-dielectric topological metasurfaces. Appl Phys Lett 2019;114:031103.

[18] Sinev IS, Mukhin IS, Slobozhanyuk AP, et al. Mapping plasmonic topological states at the nanoscale. Nanoscale 2015;7:11904–8.

[19] Kruk S, Slobozhanyuk A, Denkova D, et al. Edge states and topological phase transitions in chains of dielectric nanoparticles. Small 2017;13:1603190.

[20] Hasan MZ, Kane CL. Colloquium: topological insulators. Rev Mod Phys 2010;82:3045.

[21] Ozawa T, Price HM, Amo A, et al. Topological photonics. Rev Mod Phys 2019;91:015006.

[22] Rider MS, Palmer SJ, Pocock SR, Xiao X, Huidobro PA, Giannini V. A perspective on topological nanophotonics: current status and future challenges. J Appl Phys 2019;125:120901.

[23] Blanco de Paz M, Vergniory MG, Bercioux D, García-Etxarri A, Bradlyn B. Engineering fragile topology in photonic crystals: topological quantum chemistry of light. Phys Rev Res 2019;1:032005.

[24] Wang Z, Chong Y, Joannopoulos JD, Soljačić M. Observation of unidirectional backscattering-immune topological electromagnetic states. Nature 2009;461:772–5.

[25] Jin D, Christensen T, Soljačić M, Fang NX, Lu L, Zhang X. Infrared topological plasmons in graphene. Phys Rev Lett 2017;118:245301.

[26] Qian K, Apigo DJ, Prodan C, Barlas Y, Prodan E. Topology of the valley-Chern effect. Phys Rev B 2018;98:155138.

[27] Gao F, Xue H, Yang Z, et al. Topologically protected refraction of robust kink states in valley photonic crystals. Nat Phys 2018;14:140–4.

[28] Gao Z, Yang Z, Gao F, et al. Valley surface-wave photonic crystal and its bulk/edge transport. Phys Rev B 2017;96:201402.

[29] Dong J-W, Chen X-D, Zhu H, Wang Y, Zhang X. Valley photonic crystals for control of spin and topology. Nat Mater 2017;16:298–302.

[30] Ma T, Shvets G. All-Si valley-Hall photonic topological insulator. N J Phys 2016;18:025012.

[31] Chen X-D, Zhao F-L, Chen M, Dong J-W. Valley-contrasting physics in all-dielectric photonic crystals: orbital angular momentum and topological propagation. Phys Rev B 2017;96:020202.

[32] Jung M, Fan Z, Shvets G. Midinfrared plasmonic valleytronics in metagate-tuned graphene. Phys Rev Lett 2018;121:086807.

[33] Wu X, Meng Y, Tian J, et al. Direct observation of valley-polarized topological edge states in designer surface plasmon crystals. Nat Commun 2017;8:1304.

[34] Makwana MP, Craster RV. Designing multidirectional energy splitters and topological valley supernetworks. Phys Rev B 2018;98:235125.

[35] Makwana MP, Craster RV. Geometrically navigating topological plate modes around gentle and sharp bends. Phys Rev B 2018;98:184105.

[36] Yang HU, D'Archangel J, Sundheimer ML, Tucker E, Boreman GD, Raschke MB. Optical dielectric function of silver. Phys Rev B 2015;91:235137.

[37] Weber W, Ford G. Propagation of optical excitations by dipolar interactions in metal nanoparticle chains. Phys Rev B 2004;70:125429.

[38] Wang L, Zhang R-Y, Xiao M, Han D, Chan CT, Wen W. The existence of topological edge states in honeycomb plasmonic lattices. N J Phys 2016;18:103029.

[39] Pocock SR, Huidobro PA, Giannini V. Bulk-edge correspondence and long-range hopping in the topological plasmonic chain. Nanophotonics 2019;8:1337–47.

[40] Lu J, Qiu C, Xu S, Ye Y, Ke M, Liu Z. Dirac cones in two-dimensional artificial crystals for classical waves. Phys Rev B 2014;89:134302.

[41] Zhu H, Liu T-W, Semperlotti F. Design and experimental observation of valley-Hall edge states in diatomic-graphene-like elastic waveguides. Phys Rev B 2018;97:174301.

[42] Ma T, Shvets G. Scattering-free edge states between heterogeneous photonic topological insulators. Phys Rev B 2017;95:165102.

[43] Han D, Lai Y, Zi J, Zhang Z-Q, Chan CT. Dirac spectra and edge states in honeycomb plasmonic lattices. Phys Rev Lett 2009;102:123904.

[44] Saba M, Hamm JM, Baumberg JJ, Hess O. Group theoretical route to deterministic Weyl points in chiral photonic lattices. Phys Rev Lett 2017;119:227401.

[45] Zhen Y-R, Fung KH, Chan C. Collective plasmonic modes in two-dimensional periodic arrays of metal nanoparticles. Phys Rev B 2008;78:035419.

[46] Chen Q, Zhang L, He M, et al. Valley-Hall photonic topological insulators with dual-band kink states. Adv Opt Mater 2019;7:1900036.

[47] Zhang Z, Gu Y, Long H, Cheng Y, Liu X, Christensen J. Subwavelength acoustic valley-Hall topological insulators using soda cans honeycomb lattices. Research 2019;2019:5385763.

[48] Sakoda K. Photonic Dirac cones realized by accidental degeneracy on the Brillouin-zone boundary. Int J Mod Phys B 2014;28:1441008.

[49] He W-Y, Chan C. The emergence of Dirac points in photonic crystals with mirror symmetry. Sci Rep 2015;5:8186.

[50] Makwana MP, Chaplain GJ. Tunable three-way topological energy-splitter: venturing beyond graphene-like structures. Sci Rep 2019;9:18939.

[51] Silveirinha MG. Proof of the bulk-edge correspondence through a link between topological photonics and fluctuation-electrodynamics. Phys Rev X 2019;9:011037.

[52] Yang Y, Jiang H, Hang ZH. Topological valley transport in two-dimensional honeycomb photonic crystals. Sci Rep 2018;8:1588.

[53] Bliokh KY, Bekshaev AY, Nori F. Optical momentum, spin, and angular momentum in dispersive media. Phys Rev Lett 2017;119:073901.

[54] Bi X, Jung J, Qiao Z. Role of geometry and topological defects in the one-dimensional zero-line modes of graphene. Phys Rev B 2015;92:235421.

[55] Wu L-H, Hu X. Scheme for achieving a topological photonic crystal by using dielectric material. Phys Rev Lett 2015;114:223901.

[56] Orazbayev B, Fleury R. Quantitative robustness analysis of topological edge modes in C6 and valley-Hall metamaterial waveguides. Nanophotonics 2019;8:1433–41.